 Research Article

applied optics

Femtosecond laser-plasma dynamics study by a time-resolved Mach–Zehnder-like interferometer

Armando Valter Felicio Zuffi,[1] Jhonatha Ricardo dos Santos,[1] Edison Puig Maldonado,[2] Nilson Dias Vieira Jr.,[1] and Ricardo Elgul Samad[1,*]

[1]Instituto de Pesquisas Energéticas e Nucleares–IPEN-CNEN, Av. Prof. Lineu Prestes, 2242, 05508-000, São Paulo, SP, Brazil
[2]Instituto Tecnológico de Aeronáutica–ITA, Pç. Mal. Eduardo Gomes, 50 Vila das Acácias, 12228-615 São José dos Campos, SP, Brazil
*resamad@gmail.com

Received 4 October 2022; revised 23 December 2022; accepted 23 January 2023; posted 25 January 2023; published 22 February 2023

Side-view density profiles of a laser-induced plasma were measured by a home-built, time-resolved, Mach–Zehnder-like interferometer. Due to the pump-probe femtosecond resolution of the measurements, the plasma dynamics was observed, along with the pump pulse propagation. The effects of impact ionization and recombination were evidenced during the plasma evolution up to hundreds of picoseconds. This measurement system will integrate our laboratory infrastructure as a key tool for diagnosing gas targets and laser-target interaction in laser wakefield acceleration experiments.

https://doi.org/10.1364/AO.477395

1. INTRODUCTION

Over the last few decades, the ongoing development of compact particle accelerators based on laser wakefield acceleration (LWFA) has been promoting contributions in fundamental and applied research [1,2], including a possible future use in the production of radioisotopes for nuclear medicine [3,4], and in proton therapy and hadron therapy [5,6]. This approach uses high-intensity laser pulses focused on a gas target to create a plasma wave in which longitudinal electric fields efficiently accelerate electrons [7,8]. The advances in high-peak-power tabletop lasers in the last decades, together with the high longitudinal electric fields (up to ∼1 TV/m) supported by plasma waves, attracted attention to LWFA as a compact alternative for RF conventional accelerators [9], which can support only ∼100 MV/m due to the accelerator materials breakdown [10]. Recent experiments demonstrated the acceleration of electrons to a few gigaelectron volts in distances as short as 20 cm using lasers with peak powers from 0.3 to 0.85 PW [11,12], in a laboratory room scale. This result represents a significant reduction in the accelerator size and cost, as well as a promising outlook for LWFA.

In light of this encouraging scenario, many groups worldwide have been pursuing advances in the LWFA field and other plasma acceleration schemes, from institutions across North America, Europe, and Asia [2]. In Latin America, our research group has worked to pioneer the implementation of a laser-plasma accelerator at the Nuclear and Energy Research Institute (IPEN) [13]. The main goal of this proposal is to produce electron bunches with energy up to tens of megaelectron volts by LWFA. Those electrons would be used to generate γ-radiation by bremsstrahlung, with enough energy to induce the photonuclear reaction ^{100}Mo (γ, n) ^{99}Mo as a future application [14]. For this aim, we are currently focusing efforts on several developments required for a LWFA installation, such as computational simulation support [15–17], a source of high-peak-power laser pulses [18], proper gaseous and plasma target creation [19,20], and development and implementation of diagnostic tools to assist and monitor the experiments [21,22]. This last requirement is crucial because instabilities in both the targets and the laser pulses can result in low reproducibility of the LWFA processes and impair the accelerated electron bunches quality [23]. These diagnostics also are of major importance to a better understanding of the laser-plasma interaction. Therefore, the need for diagnostic tools, especially those that respond in the timeframe of the pulse duration (tens of femtoseconds), has been drawing increasing attention [24–26]. Furthermore, a large part of the effort to have a LWFA infrastructure running is directed to diagnostic systems, which consume approximately 10% of the installation budget [27].

Several non-disturbing optical methods can be used to diagnose the gaseous target, laser-induced plasma, and electron bunches, such as interferometry [28], Schlieren imaging [29], spectroscopy [30], and fluorescence techniques [31]. Among them, interferometry is a very accurate technique capable of quantifying very small optical path differences and therefore suitable for measuring density variations in LWFA targets [32,33]. From an interferometry measurement (interferogram), the phase shift accumulated by a laser beam propagating through a gaseous target or plasma can be extracted and, consequently, their density distributions can be determined. While a continuously flowing gaseous target can be diagnosed by

CW interferometry, analyzing a plasma created by ultrashort laser pulses requires time-resolved techniques [27] due to the short plasma formation time and fast decay of the excited ions [34], which would fade the signal in CW techniques due to the extremely small duty cycle. In this scope, the interferometry made with femtosecond temporal resolution is a powerful diagnostic tool for LWFA, since this technique can characterize the gaseous target (continuous or pulsed flow) [35] and laser-induced plasmas [32,36,37] during the wakefield formation and electron acceleration process [38].

We developed a new time-resolved Mach–Zehnder-like interferometer (MZI) coupled to a pump-probe setup capable of diagnosing transient phenomena in gaseous targets and laser-induced plasmas on the femtosecond scale [21]. This setup allows a side view of the plasma temporal evolution during its formation and subsequent evolution, and was initially tested in atmosphere, where measurements of the laser-induced plasma dynamics in air were investigated and are presented here. Although this interferometer is intended to operate in vacuum, where the LWFA will occur, in this work, we discuss the operation of the pump-probe MZI setup in atmosphere as a preliminary characterization of the device. This step aims to establish a permanent diagnostic setup in the future laser electron acceleration installation at IPEN.

2. EXPERIMENTAL SETUP

The experiments used ultrashort pulses from a Ti:sapphire multipass CPA system (Femtolasers Femtopower Compact Pro HR/HP). These pulses have a duration of 25 fs (FWHM), are centered at 785 nm with 35 nm of bandwidth (FWHM), energy up to 650 μJ at 4 kHz repetition rate in a laser beam with $M^2 \approx 1.2$. The pump-probe setup is shown in Fig. 1. Initially, a beam sampler (BSa) extracts a fraction of the pulse energy, which is sent through a delay line (delay 1) and focused in a BBO crystal to generate second-harmonic pulses at 392 nm; these probe pulses are collimated into a ~5 mm diameter beam, which enters the MZI to transversely diagnose the plasma formed by the high-energy pulses (pump) focused in atmosphere to a ~4 μm beam waist by a 90°, 50 mm off-axis parabolic mirror (OAP) [22]. The second-harmonic pulses are used as a probe due to intrinsic advantages when compared to the fundamental wavelength: they offer double spatial phase resolution, can measure higher density plasmas due to the associated higher plasma frequency, and can be isolated from laser scatterings by the use of optical filters. The temporal delay between the pump and probe pulses is controlled by a micrometric positioning system (Newport UTS100C) with a range of 200 mm and a minimum step of 1 μm, which corresponds to a double-pass minimum delay of 6.6 fs. However, the temporal resolution of the technique is limited by the duration of the probe pulses.

In the interferometer, the probe pulses are divided by a beam splitter (BS1) into reference (REF) and diagnostic (DIAG) beams. The DIAG pulses propagate through the target (plasma), and the accumulated phase can be retrieved by interference with the REF pulses, after recombination in the BS2 beam splitter. The temporal overlap between REF and DIAG pulses is obtained by adjusting the REF arm delay (delay 2) by a translation stage supporting two mirrors in a roof

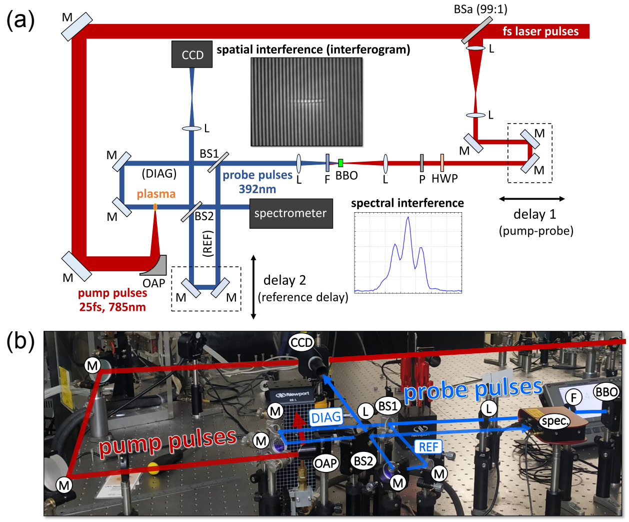

Fig. 1. (a) Schematic pump-probe setup containing the MZI. M, mirror; L, lens; F, filter; P, polarizer; BS, beam splitter; BSa, beam sampler; OAP, off-axis parabolic mirror; HWP, half-wave plate; BBO, beta barium borate crystal; CCD, charge-coupled device; and spec., spectrometer. (b) Photo of the setup.

configuration. After the BS2, the recombined pulses propagate through a 150 mm convergent lens that produces a three-fold magnified interferogram (spatial interference) at the CCD, from which the side-view plasma density can be retrieved. BS2 also directs other recombined beams to a spectrometer, creating a spectral fringe pattern (spectral interference). This spectral interference pattern is easier to find than the spatial one when adjusting the delay 2, and it is used to set the two arms with the same optical length; once this "zero-delay" position is found, the interferogram is seen on the CCD. The interferometer also allows small adjustments in the REF arm mirrors to define the fringe spatial frequency and direction.

The relevance of using a spectral interference pattern (fringes) becomes clear when comparing the pulses spatial and spectral coherence lengths. To estimate the spatial coherence length of the MZI, the contrast of the spatial interferogram fringes was plotted as a function of small displacements around the "zero-delay" position. Figure 2(a) presents a set of those interferograms, with the displacements from the "zero-delay" position indicated, and Fig. 2(b) shows the fringe contrast dependence on this displacement, and it can be clearly seen that for displacements above ~15 μm the fringes disappear. The FWHM of the fitted Gaussian function, 14.3 μm, was taken as the MZI spatial coherence length. In practice, finding the "zero-delay" position requires adjusting delay 2 within a few tens of micrometers of it, and a few micrometers are required to optimize the fringe contrast. We observe that it is very difficult to find these interference patterns experimentally.

Regarding the spectral coherence length, Fig. 3 presents the REF and DIAG beam spectral interference as a function of the displacement around the "zero-delay" position (indicated in each spectrum). These spectra plainly show that the spectral coherence length is over 200 μm, more than an order of magnitude longer than the spatial one. This happens because the spectral interference occurs even before the pulses overlap temporally [39,40] since the pulse replicas, which are apart by a time

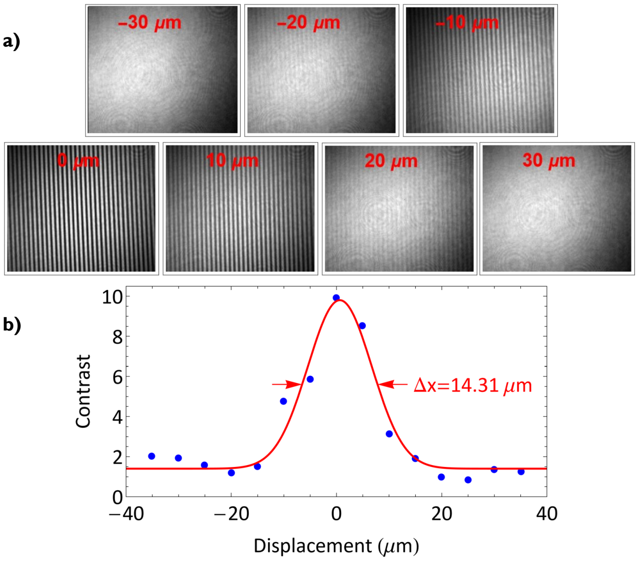

Fig. 2. Spatial-domain coherence length estimative. (a) Interferograms measured for different displacements around the "zero-delay" position. (b) Fringe contrast dependence on the displacement measured from a common line of the interferograms and fitted Gaussian.

τ in the time domain print a spectral fringe with the period of $1/\tau$ over the pulse spectra in the frequency domain. Using this concept, we have enhanced the handling of the setup, making it easier to find the "zero-delay" position for the REF arm to measure the interferograms at the CCD.

3. INTERFEROGRAM ANALYSIS

The inset in Fig. 1 shows a typical interferogram of the plasma side view recorded by the MZI. The phase shift accumulated by the DIAG pulses propagating through the plasma shifts the interferogram fringes [33], and a mathematical process is used to retrieve the plasma density profile. A workflow commonly used to retrieve plasma density consists of (1) obtaining an interferogram of the background (bg) and another of the background+target (bg + t), the laser-induced plasma in this case; (2) transforming both interferograms to the frequency domain by 2D Fourier transforms; (3) applying a filter over the region that contains the target phase-shift information [41] in both frequency domain maps; (4) performing an inverse Fourier transform to the filtered frequency domain maps, generating the bg and bg + t phase-shift maps; (5) subtracting the bg phase-shift map from the bg + t map, to obtain the target integrated phase-shift map [41,42], or simply $\Delta\phi_x$ map. This map contains the integrated phase along the DIAG beam propagation direction (x direction), and assuming an axisymmetric plasma, the integrated information along x is sufficient to reconstruct the radial information $\Delta\phi_r$ using inversion techniques, such as the Abel inversion method [42,43]:

$$\Delta\phi_x = 2\int_x^{\infty} \frac{r\,\Delta\phi_r}{\sqrt{r^2 - x^2}}\mathrm{d}r, \tag{1}$$

which is generally used, considering that imperfections in the cylindrical symmetry of real targets are second-order corrections and can be neglected. Although the Abel inversion method is also recommended to reconstruct the plasma density profile, we decided not to use it for the analysis of our interferograms, and to present and discuss the raw data. Due to the small plasma length and radial distribution (both in the tens of micrometer scale), we believe that this procedure will not significantly affect our final analyses and conclusions.

Starting from the $\Delta\phi_x$ map, the x-direction integrated refractive index of the plasma, n_p, can be obtained by

$$n_p = 1 + \frac{\Delta\phi_x \lambda_L}{2\pi l}, \tag{2}$$

where λ_L is the wavelength of the laser inspecting the plasma, and l is the $1/e^2$ diameter of the plasma, which is estimated from the phase-shift map assuming a cylindrical symmetry. Moreover, the plasma electronic density, n_e, can be evaluated from the plasma refractive index by [44]

$$\begin{aligned} n_e &= \frac{4\pi^2 c^2 \varepsilon_0 m_e}{e^2\lambda_L^2}\left(1 - n_p^2\right) \\ &= \frac{4\pi^2 c^2 \varepsilon_0 m_e}{e^2\lambda_L^2}\left[1 - \left(1 + \frac{\Delta\phi_x\lambda_L}{2\pi l}\right)^2\right], \end{aligned} \tag{3}$$

where e and m_e are the electron charge and mass, c is the speed of light in a vacuum, and ε_0 is the vacuum permittivity. This simple

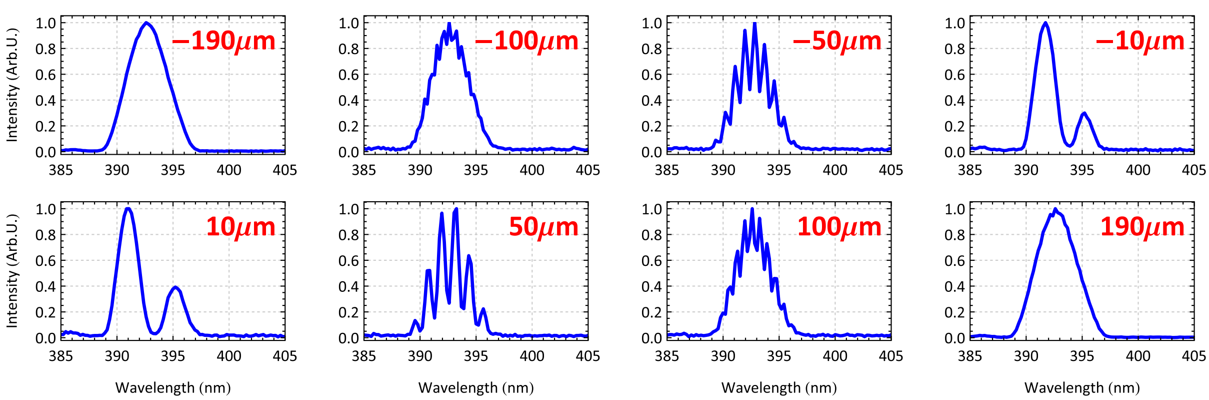

Fig. 3. Spectral-domain coherence length performed from the spectra measured with different values of delay 2. The spectral interference pattern appears for delay times by an order of magnitude greater than that for spatial interference.

model assumes that there is no variation of n_e across the plasma diameter due to differences in the local number of ionizations.

The plasma densities were calculated by (3) from interferograms obtained with $\lambda_L = (392 \pm 2)$ nm and $l = (20 \pm 2)$ µm. These uncertainties were obtained considering that the laser wavelength is the mean value of a Gaussian spectrum with ∼25 nm of bandwidth, and the CCD pixel size calibration for the plasma diameter. Additionally, from different interferograms obtained for the same plasma, we estimated the phase-shift uncertainty to be $\sigma_{\Delta\phi_x} = 0.05\Delta\phi_x$ (5% of the retrieved phase), also impacting the results from (3).

4. LASER-INDUCED PLASMA CHARACTERIZATION

A. Plasma Formation in Air

Plasma was formed in air by focusing 200 µJ, 25 fs pulses to intensities above 10^{16} W/cm^2 [22]. The interferogram fringes were adjusted to be perpendicular to the laser propagation direction, and with a spatial frequency sufficiently high to make the plasma shifted fringes clearly visible.

Figure 4 presents the plasma density temporal evolution for six different delays after the plasma formation (100, 300, 500, 700, 900, and 1100 fs). The zero-time was defined, with an uncertainty of tens of femtoseconds, when the interferogram displayed small fringe shifts near the expected plasma region. Figure 4(a) presents the plasma size and position, retrieved from the interferograms, as a function of time (shown in the labels), which can be correlated to the laser pulse propagation (also in labels). Figure 4(b) presents the plasma $1/e^2$ length and maximum density obtained from the maps shown in (a), where it can be observed that the plasma peak density increases up to a maximum of $(3.2 \pm 0.4) \times 10^{19}$ cm^{-3}, and its longitudinal length reaches a (225 ± 23) µm maximum, close to the OAP defined confocal parameter.

Assuming that air is composed of 80% N_2 and 20% O_2, and that its number density at room temperature (300 K) and 1 atm is 2.5×10^{19} cm^{-3}, we can estimate its expected ionization for the applied laser intensity. At the temporal scales and intensities explored in Fig. 4, ionization occurs for atoms that are not resonant with the laser wavelength mainly through three nonlinear processes, presented in increasing intensity order: multiphoton ionization, tunneling ionization [45], and barrier suppression ionization (BSI) [46]. We consider here, in a simplified way, that ionization occurs only when the intensity overcomes the BSI threshold, I_{th}, given by [46,47]

Table 1. Ionization Energies (E_{ion}) and BSI Intensity Thresholds (I_{th}) for Nitrogen and Oxygen Atoms

	Nitrogen		Oxygen	
Ionization State	E_{ion} (eV)	I_{th} (W/cm^2)	E_{ion} (eV)	I_{th} (W/cm^2)
+1	14.53	1.8×10^{14}	13.62	1.4×10^{14}
+2	29.60	7.7×10^{14}	35.12	1.5×10^{15}
+3	47.45	2.3×10^{15}	54.94	4.0×10^{15}
+4	77.48	9.0×10^{15}	77.41	9.0×10^{15}
+5	97.89	1.5×10^{16}	113.90	2.7×10^{16}
+6	552.1	1.0×10^{19}	138.2	4.0×10^{16}
+7	667.1	1.6×10^{19}	739.28	2.4×10^{19}
+8	–	–	871.41	3.6×10^{19}

$$I_{th}\left(\frac{W}{cm^2}\right) = 4.00 \times 10^9 \frac{E_{ion}^4\,(eV)}{Z^2}, \tag{4}$$

where E_{ion} is the atom ionization energy in eV, and Z is its ionization state; Table 1 presents the intensity thresholds for all nitrogen and oxygen ionizations.

Considering that the laser pulses are in a TEM_{00} Gaussian beam, the intensity at the focus is $(1.2 \pm 0.3) \times 10^{16}$ W/cm^2, enough to dissociate the N_2 and O_2 molecules, and to ionize their atoms four times, creating a plasma with an electronic density of 2×10^{20} cm^{-3}. The peak intensity of the pulses is $(2.3 \pm 0.5) \times 10^{16}$ W/cm^2 sufficient to ionize the nitrogen, but not the oxygen, to the 5+ state; taking the air composition into consideration, the plasma peak density can be as high as 2.4×10^{20} cm^{-3}. These predicted density values are 6.3 and 7.5 times higher than the $(3.2 \pm 0.4) \times 10^{19}$ cm^{-3} measured. Similar discrepancies are reported in the literature when using interferometry [48,49], and the most probable causes for this disagreement are related to the expected electron density and the density recovery algorithm. Regarding the theoretical expected density, our simple estimate may have overestimated its value, since we assumed a constant intensity (apart from the peak intensity) and did not consider the laser intensity spatial profile, which would decrease the air ionization state in the beam wings due to lower intensities, resulting in a smaller integrated density [33]. Additionally, processes that mitigate the laser intensity, such as plasma defocusing near the focus [50,51], could impair the ionization processes, reducing the free electron density. Additionally, our retrieval algorithm returned the integrated electronic density, but not its spatial profile, which would increase the peak value. We are currently working to implement

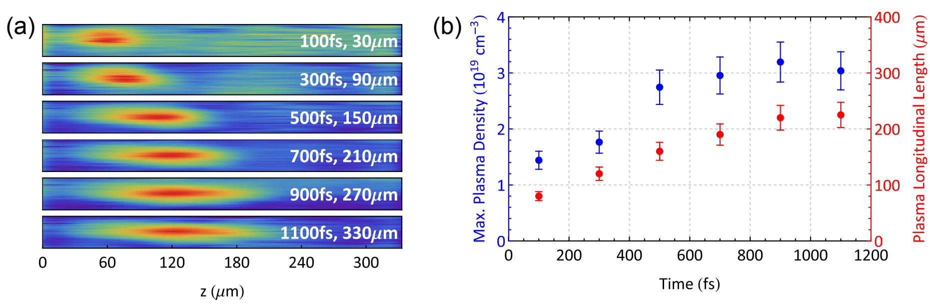

Fig. 4. (a) Side-view plasma density maps for six different delays after plasma formation. Labels: delay and the corresponding pulse propagation position. (b) Temporal evolution of the plasma peak density and length.

a reliable Abel inversion algorithm to obtain the density spatial distribution. Finally, we are still devising ways to overcome difficulties associated with loss of contrast in the interferogram due to the modulations caused by the plasma. This effect causes an effective decrease in the measured phase shift, since the resultant fringes are normalized by the lower ionization states that occupy a larger plasma region [32]. Although these problems must be overcome to allow absolute measurements of plasma density, the interferometer described here has good characteristics and is already in use for the characterization of relative density changes in generated plasmas as a function of time.

B. Plasma Evolution in Air

Another application of the MZI is to explore the laser-induced plasma evolution after its formation. In this investigation, the experimental conditions were the same as previously described. The maximum plasma density was measured after the plasma formation for delays ranging from 50 fs to 0.8 ns (maximum delay in our setup). At this time interval, the plasma thermal effects are present, as well as possible recombination dynamics, since femtosecond laser-induced plasmas in the air have a lifetime of a few nanoseconds [52], and it is possible to estimate the plasma temperature. To be able to do this, a local thermal equilibrium (LTE) has to exist attending the McWhirter criterion [53,54]:

$$n_e \geq 1.6 \times 10^{12}\sqrt{T}\left(\Delta E_{ij}\right)^3, \tag{5}$$

where T is the plasma temperature in K, and ΔE_{ij} is the energy difference between the transition levels i and j, with $i > j$, in eV. This criterion establishes a minimum local density to attain the LTE by collisional processes and can be used for ultrashort pulses originated plasmas [55]. As discussed in the previous section, since is estimated that nitrogen is fully ionized to the state +4 and, when close to the laser peak, it can reach the state +5, these two states were considered, resulting in $\Delta E_{ij} = 20.4$ eV. For temperatures under 100,000 K, (5) states that the electronic density must be greater than $\sim 4.3 \times 10^{18}$ cm^{-3}, as is the case.

With these considerations, it is possible to estimate the plasma temperature from the maximum plasma density by applying the Saha equation [56]:

$$\frac{n_e n_i}{n_j} = \frac{2(2\pi m_e k T)^{3/2}}{h^3}\frac{U_i\,(T)}{U_j\,(T)}\exp\left(-\frac{\Delta E_{ij}}{kT}\right), \tag{6}$$

where n_e is the plasma electrons density, n_i and n_j are the ionic densities in states i and j, respectively, T is the plasma temperature, h is the Planck constant, k is the Boltzmann constant, and $U_i(T)$ and $U_j(T)$ are the ionic partition functions for the states i and j in the LTE. To estimate the plasma temperature, the nitrogen population on the +5 state was assumed to be 20% of the +4 population ($n_i/n_j = 0.2$), and the partition functions were obtained from the NIST Atomic Spectra Database [57], assuming $T = 30,000$ K. The estimated temperature evolution was obtained from the plasma maximum electronic density evolution, and the results are shown in Fig. 5.

The results presented in Fig. 5 show an increasing trend in the maximum plasma density up to $(6.1 \pm 0.7) \times 10^{19}$ cm^{-3} at about 15 ps, a much longer time than the pulse propagation period through the confocal region of the laser beam. This ~90% increase over the maximum plasma density reported in Fig. 4 indicates plasma formation by a process other than photoionization, since the laser pulse is not at the plasma region at these times. Therefore, impact ionization (collisional ionization) should be investigated [58,59]. In addition, beyond 15 ps, the maximum plasma density decreases, which indicates that electron-ion recombination effects begin to be predominant [52,60].

The estimated plasma temperature evolution follows the same behavior as the plasma density, with a peak of $(33{,}700 \pm 400)$ K at ~15 ps. Regarding the ionic population ratio, its value was assumed to be $n_i/n_j = 0.2$, but it could vary from 0.1 up to 0.4, changing the estimated temperature by less than 10%. Additionally, the partition functions could have been taken at any temperature between 10,000 and 50,000 K, and the estimated plasma temperature would change by no more than 3%, so after a few interactions we choose to use the partition functions at 30,000 K because this value is closer to the estimated plasma temperature along its evolution. Despite all this, the plasma temperature obtained is only an estimate, and it was calculated considering exclusively the nitrogen atoms because, in the simple BSI model adopted, all oxygen atoms are ionized to the final +4 state, with no population on the +5 state, so the Saha equation cannot be applied to this species. To consider the oxygen, better population estimates, based on more complex ionization models and spatial distributions, would have to be used, but the values obtained give us an assessment of the temperatures reached by the plasma.

Although time delays longer than 0.8 ns could not be explored in this experimental setup, the density and temperature decreasing trends should become more evident, as longer

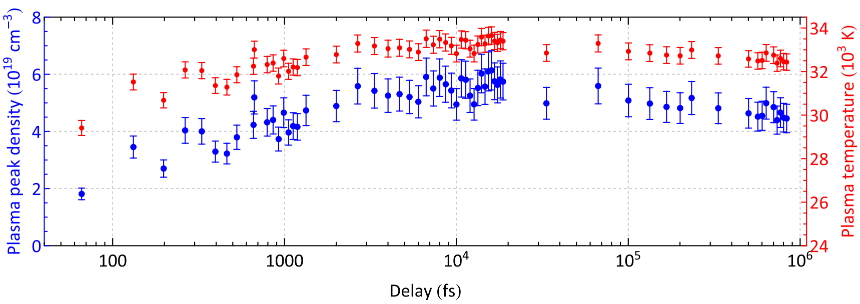

Fig. 5. Temporal evolution of laser-induced plasma maximum densities (blue) and temperatures (red).

times allow for more electron recombinations and cooling to the surrounding environment.

5. CONCLUSION

We developed and built a time-resolved MZI that was used to diagnose laser-induced plasmas, allowing side-view interferograms with micrometric and femtosecond resolutions. Using this setup, we investigated the plasma evolution in air, where the MZI's characteristics could be explored during plasma formation (nonthermal dynamics) and evolution to longer times (thermal dynamics). Although discrepancies in the plasma density values between theoretical predictions and experimental measurements were observed, the findings exhibited in this work demonstrate the suitability of this instrumentation to diagnose plasma dimensions and density gradients. Measurements of plasma in air are important to provide a better understanding of the plasma dynamics when generated by ultrashort laser pulses, aiming to establish a permanent diagnostic setup for further LWFA experiments at IPEN.

Funding. Fundação de Amparo à Pesquisa do Estado de São Paulo (FAPESP) (17/50332-0, 21/13737-8); Conselho Nacional de Desenvolvimento Científico e Tecnológico (CNPq) (465763/2014-6, 142246/2018-2).

Acknowledgment. Portions of this work were presented at the Latin America Optics and Photonics Conference (LAOP) in 2022, paper number Tu4A.49. The authors are grateful for the FAPESP scholarship (to J. R. dos Santos) and the CNPq scholarship (to A. V. F. Zuffi).

Disclosures. The authors declare no conflicts of interest.

Data availability. Data underlying the results presented in this paper are not publicly available at this time but may be obtained from the authors upon reasonable request.

REFERENCES

1. F. Albert, "Laser wakefield accelerators: next-generation light sources," Opt. Photonics News **29**(1), 42–49 (2018).
2. F. Albert, M. E. Couprie, A. Debus, *et al.*, "2020 roadmap on plasma accelerators," New J. Phys. **23**, 031101 (2021).
3. K. Nemoto, A. Maksimchuk, S. Banerjee, K. Flippo, G. Mourou, D. Umstadter, and V. Y. Bychenkov, "Laser-triggered ion acceleration and table top isotope production," Appl. Phys. Lett. **78**, 595–597 (2001).
4. I. Spencer, K. W. D. Ledingham, R. P. Singhal, T. McCanny, P. McKenna, E. L. Clark, K. Krushelnick, M. Zepf, F. N. Beg, M. Tatarakis, A. E. Dangor, P. A. Norreys, R. J. Clarke, R. M. Allott, and I. N. Ross, "Laser generation of proton beams for the production of short-lived positron emitting radioisotopes," Nucl. Instrum. Methods B **183**, 449–458 (2001).
5. K. Ledingham, P. Bolton, N. Shikazono, and C. M. Ma, "Towards laser driven Hadron cancer radiotherapy: a review of progress," Appl. Sci. **4**, 402–443 (2014).
6. A. Giulietti, *Laser-Driven Particle Acceleration Towards Radiobiology and Medicine*, Biological and Medical Physics, Biomedical Engineering (Springer International Publishing, 2016).
7. E. Esarey, C. B. Schroeder, and W. P. Leemans, "Physics of laser-driven plasma-based electron accelerators," Rev. Mod. Phys. **81**, 1229–1285 (2009).
8. T. Tajima and J. M. Dawson, "Laser electron-accelerator," Phys. Rev. Lett. **43**, 267–270 (1979).
9. S. M. Hooker, "Developments in laser-driven plasma accelerators," Nat. Photonics **7**, 775–782 (2013).
10. A. W. Chao and M. Tigner, *Handbook of Accelerator Physics and Engineering* (World Scientific, 1999).
11. A. J. Gonsalves, K. Nakamura, J. Daniels, *et al.*, "Petawatt laser guiding and electron beam acceleration to 8 GeV in a laser-heated capillary discharge waveguide," Phys. Rev. Lett. **122**, 084801 (2019).
12. B. Miao, J. E. Shrock, L. Feder, R. C. Hollinger, J. Morrison, R. Nedbailo, A. Picksley, H. Song, S. Wang, J. J. Rocca, and H. M. Milchberg, "Multi-GeV electron bunches from an all-optical laser wakefield accelerator," Phys. Rev. X **12**, 031038 (2022).
13. N. D. Vieira, R. E. Samad, and E. P. Maldonado, "Compact laser accelerators towards medical applications—perspectives for a Brazilian Program," in *SBFoton International Optics and Photonics Conference* (IEEE, 2019).
14. N. D. Vieira, E. P. Maldonado, A. Bonatto, R. P. Nunes, S. Banerjee, F. A. Genezini, M. Moralles, A. V. F. Zuffi, and R. E. Samad, "Laser wakefield electron accelerator: possible use for radioisotope production," in *SBFoton International Optics and Photonics Conference* (IEEE, 2021).
15. E. P. Maldonado, R. E. Samad, A. Bonatto, R. P. Nunes, S. Banerjee, and N. D. Vieira, "Study of quasimonoenergetic electron bunch generation in self-modulated laser wakefield acceleration using TW or sub-TW ultrashort laser pulses," AIP Adv. **11**, 065116 (2021).
16. E. P. Maldonado, R. E. Samad, A. Bonatto, R. P. Nunes, S. Banerjee, and N. D. Vieira, "Electron beam properties in self-modulated laser wakefield acceleration using TW and sub-TW pulses," in *SBFoton International Optics and Photonics Conference* (IEEE, 2021).
17. E. P. Maldonado, R. E. Samad, A. V. F. Zuffi, F. B. D. Tabacow, and N. D. Vieira, "Self-modulated laser-plasma acceleration in a H_2 gas target, simulated in a spectral particle-in-cell algorithm: wakefield and electron bunch properties," in *SBFoton International Optics and Photonics Conference* (IEEE, 2019).
18. R. E. Samad, E. P. Maldonado, W. De Rossi, and N. D. V. Junior, "High intensity ultrashort laser pulses and their applications at IPEN," in *SBFoton International Optics and Photonics Conference* (IEEE, 2021).
19. B. B. Chiomento, A. V. F. Zuffi, N. D. V. Junior, F. B. D. Tabacow, E. P. Maldonado, and R. E. Samad, "Development of dielectric de Laval nozzles for laser electron acceleration by ultrashort pulses micromachining," in *SBFoton International Optics and Photonics Conference* (IEEE, 2021).
20. F. B. D. Tabacow, A. V. F. Zuffi, E. P. Maldonado, R. E. Samad, and N. D. Vieira, "Theoretical and experimental study of supersonic gas jet targets for laser wakefield acceleration," in *SBFoton International Optics and Photonics Conference* (IEEE, 2021).
21. A. V. F. Zuffi, E. P. Maldonado, N. D. Vieira, and R. E. Samad, "Development of a modified Mach-Zehnder interferometer for time and space density measurements for laser wakefield acceleration," in *SBFoton International Optics and Photonics Conference* (IEEE, 2021).
22. R. E. Samad, A. V. F. Zuffi, E. P. Maldonado, and N. D. Vieira, "Development and optical characterization of supersonic gas targets for high-intensity laser plasma studies," in *SBFoton International Optics and Photonics Conference* (IEEE, 2018).
23. P. Sprangle, B. Hafizi, and J. R. Peñano, "Laser pulse modulation instabilities in plasma channels," Phys. Rev. E **61**, 4381–4393 (2000).
24. T. Chagovets, S. Stanček, L. Giuffrida, A. Velyhan, M. Tryus, F. Grepl, V. Istokskaia, V. Kantarelou, T. Wiste, J. C. Hernandez Martin, F. Schillaci, and D. Margarone, "Automation of target delivery and diagnostic systems for high repetition rate laser-plasma acceleration," Appl. Sci. **11**, 1680 (2021).
25. R. Zaffino, M. Seimetz, D. Quirión, A. R. De La Cruz, I. Sánchez, P. Mur, J. Benlliure, L. Martín, L. Roso, J. M. Benlloch, M. Lozano, and G. Pellegrini, "Preparation and characterization of micro-nano engineered targets for high-power laser experiments," Microelectron. Eng. **194**, 67–70 (2018).
26. I. Prencipe, J. Fuchs, S. Pascarelli, *et al.*, "Targets for high repetition rate laser facilities: needs, challenges and perspectives," High P. Las. Sci. Eng. **5**, E17 (2017).
27. M. C. Downer, R. Zgadzaj, A. Debus, U. Schramm, and M. C. Kaluza, "Diagnostics for plasma-based electron accelerators," Rev. Mod. Phys. **90**, 035002 (2018).
28. G. Costa, M. P. Anania, F. Bisesto, E. Chiadroni, A. Cianchi, A. Curcio, M. Ferrario, F. Filippi, A. Marocchino, F. Mira, R. Pompili, and A. Zigler,

"Characterization of self-injected electron beams from LWFA experiments at SPARC_LAB," Nucl. Instrum. Methods A **909**, 118–122 (2018).
29. G. S. Settles, Schlieren and shadowgraph techniques: visualizing phenomena in transparent media, in *Experimental Fluid Mechanics* (Springer, 2001), pp. xviii.
30. S. Shiraishi, C. Benedetti, A. J. Gonsalves, K. Nakamura, B. H. Shaw, T. Sokollik, J. van Tilborg, C. G. R. Geddes, C. B. Schroeder, C. Toth, E. Esarey, and W. P. Leemans, "Laser red shifting based characterization of wakefield excitation in a laser-plasma accelerator," Phys. Plasmas **20**, 063103 (2013).
31. A. J. Goers, G. A. Hine, L. Feder, B. Miao, F. Salehi, J. K. Wahlstrand, and H. M. Milchberg, "Multi-MeV electron acceleration by Subterawatt laser pulses," Phys. Rev. Lett. **115**, 194802 (2015).
32. F. Brandi and L. A. Gizzi, "Optical diagnostics for density measurement in high-quality laser-plasma electron accelerators," High Power Laser Sci. Eng. **7**, e26 (2019).
33. A. K. Arunachalam, "Investigation of laser-plasma interactions at near-critical densities," Dissertation (University of Jena, 2017).
34. D. A. Jaroszynski, R. Bingham, and R. A. Cairns, *Laser-Plasma Interactions*, Scottish Graduate Series (CRC Press/Taylor & Francis, 2009).
35. F. Brandi, P. Marsili, F. Giammanco, F. Sylla, and L. A. Gizzi, "Measurement of the particle number density in a pulsed flow gas cell with a second-harmonic interferometer," J. Phys. Conf. Ser. **1079**, 012006 (2018).
36. A. K. Arunachalam, M. B. Schwab, A. Sävert, and M. C. Kaluza, "Observation of non-symmetric side-scattering during high-intensity laser-plasma interactions," New J. Phys. **20**, 033027 (2018).
37. A. Flacco, A. Guemnie-Tafo, R. Nuter, M. Veltcheva, D. Batani, E. Lefebvre, and V. Malka, "Characterization of a controlled plasma expansion in vacuum for laser driven ion acceleration," J. Appl. Phys. **104**, 103304 (2008).
38. J. R. Marquès, J. P. Geindre, F. Amiranoff, P. Audebert, J. C. Gauthier, A. Antonetti, and G. Grillon, "Temporal and spatial measurements of the electron density perturbation produced in the wake of an ultrashort laser pulse," Phys. Rev. Lett. **76**, 3566–3569 (1996).
39. C. Dorrer, "Influence of the calibration of the detector on spectral interferometry," J. Opt. Soc. Am. B **16**, 1160–1168 (1999).
40. L. Lepetit, G. Cheriaux, and M. Joffre, "Linear techniques of phase measurement by femtosecond spectral interferometry for applications in spectroscopy," J. Opt. Soc. Am. B **12**, 2467–2474 (1995).
41. J. P. Couperus, A. Kohler, T. A. W. Wolterink, A. Jochmann, O. Zarini, H. M. J. Bastiaens, K. J. Boller, A. Irman, and U. Schramm, "Tomographic characterisation of gas-jet targets for laser wakefield acceleration," Nucl. Instrum. Meth. A **830**, 504–509 (2016).
42. V. Malka, C. Coulaud, J. P. Geindre, V. Lopez, Z. Najmudin, D. Neely, and F. Amiranoff, "Characterization of neutral density profile in a wide range of pressure of cylindrical pulsed gas jets," Rev. Sci. Instrum. **71**, 2329–2333 (2000).
43. R. Álvarez, A. Rodero, and M. C. Quintero, "An Abel inversion method for radially resolved measurements in the axial injection torch," Spectrochim. Acta B **57**, 1665–1680 (2002).
44. J. T. Verdeyen and J. B. Gerardo, "Application of laser to plasma refractive index determination," Ann. N.Y. Acad. Sci. **122**, 676–684 (1965).
45. P. K. Tiwari, G. J. H. Brussaard, M. J. van der Wiel, and V. K. Tripathi, "Laser induced tunnel ionization and electron density evolution in air," J. Phys. Soc. Jpn. **74**, 2255–2259 (2005).
46. S. Augst, D. Strickland, D. D. Meyerhofer, S. L. Chin, and J. H. Eberly, "Tunneling ionization of noble-gases in a high-intensity laser field," Phys. Rev. Lett. **63**, 2212–2215 (1989).
47. A. V. F. Zuffi, N. D. Vieira, and R. E. Samad, "Below-threshold-harmonics-generation limitation due to laser-induced ionization in noble gases," Phys. Rev. A **105**, 023112 (2022).
48. D. Batani, J. Santos, P. Forestier-Colleoni, D. Mancelli, M. Ehret, J. Trela, A. Morace, K. Jakubowska, L. Antonelli, D. del Sorbo, M. Manclossi, and M. Veltcheva, "Optical time-resolved diagnostics of laser-produced plasmas," J. Fusion Energy **38**, 299–314 (2019).
49. S. S. Harilal, M. C. Phillips, D. H. Froula, K. K. Anoop, R. C. Issac, and F. N. Beg, "Optical diagnostics of laser-produced plasmas," Rev. Mod. Phys. **94**, 035002 (2022).
50. V. V. Semak and M. N. Shneider, "Effect of power losses on self-focusing of high-intensity laser beam in gases," J. Phys. D **46**, 185502 (2013).
51. M. Mlejnek, E. M. Wright, and J. V. Moloney, "Power dependence of dynamic spatial replenishment of femtosecond pulses propagating in air," Opt. Express **4**, 223–228 (1999).
52. J. Penano, P. Sprangle, B. Hafizi, D. Gordon, R. Fernsler, and M. Scully, "Remote lasing in air by recombination and electron impact excitation of molecular nitrogen," J. Appl. Phys. **111**, 033105 (2012).
53. R. W. P. McWhirter, "Ultraviolet and X-ray spectroscopy of the solar atmosphere," in *Plasma Diagnostic Techniques*, R. H. Huddlestone and S. L. Leonard, eds. (Academic, 1965), pp. 201–264.
54. J. R. Dos Santos, J. J. Neto, N. Rodrigues, M. G. Destro, J. W. Neri, P. Bueno, and B. Christ, "Measurement of dysprosium stark width and the electron impact width parameter," Appl. Spectrosc. **73**, 203–213 (2019).
55. J. Bernhardt, W. Liu, F. Théberge, H. L. Xu, J. F. Daigle, M. Châteauneuf, J. Dubois, and S. L. Chin, "Spectroscopic analysis of femtosecond laser plasma filament in air," Opt. Commun. **281**, 1268–1274 (2008).
56. G. Bekefi, *Principles of Laser Plasmas* (Wiley, 1976).
57. A. Kramida, Y. Ralchenko, and J. Reader, and NIST ASD Team, "NIST atomic spectra database (version 5.9)," 2022, https://physics.nist.gov/asd.
58. E. Welch, D. Matteo, S. Tochitsky, G. Louwrens, and C. Joshi, "Observation of breakdown wave mechanism in avalanche ionization produced atmospheric plasma generated by a picosecond CO_2 laser," Phys. Plasmas **29**, 053504 (2022).
59. A. Filin, R. Compton, D. A. Romanov, and R. J. Levis, "Impact-ionization cooling in laser-induced plasma filaments," Phys. Rev. Lett. **102**, 155004 (2009).
60. A. Couairon and A. Mysyrowicz, "Femtosecond filamentation in transparent media," Phys. Rep. **441**, 47–189 (2007).